Experimental Investigation of Relative Permeability Upscaling from the Micro-Scale to the Macro-Scale

Semi-Annual Progress Report

Reporting Period Start Date: March 1, 2002
Reporting Period End Date: August 8, 2002

Laura J. Pyrak-Nolte, Ping Yu, JiangTao Cheng, Daiquan Chen, Nicholas Giordano, Mirela Mustata , John Coy, Nathan Cooper, and David D. Nolte

December 2002

DOE Award: DE-AC26-99BC15207

Purdue Research Foundation
Department of Physics
1396 Physics Building, Room 166
West Lafayette, Indiana 47907-1396

Abstract: The principal challenge of upscaling techniques for multi-phase fluid dynamics in porous media is to determine which properties on the micro-scale can be used to predict macroscopic flow and spatial distribution of phases at core- and field-scales. The most notable outcome of recent theories is the identification of interfacial areas per volume for multiple phases as a fundamental parameter that determines much of the multi-phase properties of the porous medium. A formal program of experimental research was begun to directly test upscaling theories in fluid flow through porous media by comparing measurements of relative permeability and capillary-saturation with measurements of interfacial area per volume. During this reporting period, we have shown experimentally that the coherence detection can be performed in a borescope. The measurement of interfacial area per volume (IAV), capillary pressure and saturation in two dimensional micro-models structures has shown the existence of a unique relationship among these hydraulic parameters for different pore geometry. The measurement of interfacial area per volume on a three-dimensional natural sample, i.e., sandstone, is essentially completed for imbibition conditions.

Table of Contents

List of Figures

List of Tables

Executive Summary

Direct experimental tests of upscaling theories in fluid flow through porous media will be made by comparing measurements of relative permeability and capillary-saturation with measurements of interfacial area per volume. These experiments are performed from the pore-scale (microns) to the core-scale (centimeters), spanning four orders of magnitude in size. Three experimental objectives provide the data for rigorous tests of upscaling theories. First, holographic laser imaging techniques will acquire pore-scale three-dimensional optical images of the pore geometry in reservoir sandstones. This technique uses unique properties of coherent light to see through drilling muds and into the sandstone. Second, laboratory micro-models with matched topological properties based on the data from the pore imaging will make it possible to measure interfacial area per volume in scientifically controlled imbibition and drainage experiments, combined with measurements of capillary-pressure-saturation data and relative permeability. Third, core-scale experiments of relative permeability and capillary-saturation, and metal casts of the pore geometry, will be compared with the pore-scale data of the first two objectives. The data from all these objectives will provide the first complete picture over such a large dynamic range. It will make it possible to answer the principal question concerning flow upscaling: which microscopic measurements are most useful for predicting macroscopic flow properties of an oil reservoir. The tangible outcome of this work will be explicit data connecting interfacial areas, or other relevant geometric micro-scale data, with macroscopic hydraulic properties. In addition, we show strong industrial interest in testing and commercializing the unique down-hole laser imaging technology that can be transferred to the oil-industry service-company sector.

During this reporting period, we have shown experimentally that coherence imaging detection can be performed through a borescope which is the first step in assessing the potential of OCI as a borehole tool. The measurement of interfacial area per volume (IAV), capillary pressure and saturation in two dimensional micro-models structures has shown the existence of a unique relationship among these hydraulic parameters for different pore geometry. The measurement of interfacial area per volume on a three-dimensional natural sample, i.e., sandstone, is essentially completed for imbibition conditions.

1.0 Introduction

1.1 Summary of Project Description

Standard expressions of multi-phase flow in porous media based on modifications of Darcy's Law (Darcy, 1856) have crippling deficiencies that make them undesirable to use for critical operations such as tertiary recovery of oil from depleted reservoirs. The primary difficulty in these empirical expressions are their violation of rigorous conservation laws. New theories based on rigorous volume averaging theorems and fundamental thermodynamic principles of phase boundaries have emerged in the past decade to replace the old empirical rules (Hassanizadeh and Gray, 1979; Gray, 1983). The most notable outcome of these theories is the identification of interfacial areas per volume for multiple phases as fundamental parameters that determine much of the multi-phase properties of the porous medium (Muccino, Gray and Ferrand, 1998).

Interfacial areas per volume provide natural descriptions of fundamental physical processes in porous media. For instance, thermodynamic energies are proportional to interfacial areas, and interfacial areas per volume represent a form of energy density. Gradients in energy densities define the dynamical pressures that drive the movement and distribution of phases within a complex topology. Interfacial areas per volume in a porous medium therefore represent a three-dimensional potential energy landscape.

Interfacial areas per volume also provide a natural yard-stick for defining the role of scale in multiphase fluid properties. The dimensional units of interfacial area per volume is a spatial frequency (inverse length) that breaks scale invariance. A useful illustration (Gray, 1998) of this scale-defining role can be made by considering an image of a pore-geometry containing only a single phase. Without a measurement scale, it is impossible to state what the physical size of the system is. However, when two phases such as water and air are both present, the length scale becomes obvious. At small scales, the water-air interface is drawn into the pore throats, while at large scales the water puddles in the large void volumes.

Therefore, the interfacial areas between phases define a length scale. Whenever a physical system has an intrinsic length scale, the physics of the system can be divided into two regimes: one where sample sizes are larger than the intrinsic length scale, and the other where information is obtained on scales smaller than the intrinsic length scale. Breaking

scale invariance makes it possible to define representative elementary volumes (REV) and to apply averaging theorems. Combining the averaging theorems with thermodynamics further constrains the possible types of constitutive equations that can rigorously describe multiphase fluid properties in porous media.

As a consequence of this theoretical framework, interfacial areas per volume (IAV) take on a more important role than simple volume saturation . This important role of IAV is clear because a single value of relative volume saturation can correspond to infinitely different distributions of two phases within the volume. Large values of IAV relate to a finely distributed phase that can block pore throats and seriously affect permeability, while small values of IAV relate to gross separations of phases, with large connected volumes of the phase that can flow unimpeded through the network. Significant numerical studies have been performed on the relationships between capillary-saturation and interfacial area. Reeves and Celia (1996) developed a numerical model that scans over repetitive imbibition and drainage while tracking the interfacial area for each loop. These studies pointed to a non-unique relationship between interfacial area and partial saturation, although a family of curves did emerge that lies within a localized part of the parameter space defined by area and saturation.

The numerical studies illustrate the importance of continued and extensive experimental studies and tests of upscaling theories, and in particular tests of the role of interfacial area per volume in determining macroscopic flow properties. While oil recovery predictions should certainly include IAV as critical parameters, it is important to test whether other microscopic parameters also contribute to the macroscopic behavior. For instance, scale invariance of interfacial areas, even over restricted length scales, could present serious challenges to the averaging theorems, and could modify the presumed role of interfacial area in determining macroscopic flow properties. The principal objective of our proposed upscaling approach is to experimentally measure many microscopic geometric parameters of the flow system over many scales, and connect these microscopic measurements with macroscopic flow behavior.

1.2 Project Objectives

The proposed work for this contract has three objectives that will provide rigorous experimental tests of upscaling theories. The objectives are:

1) To use holographic laser imaging techniques to acquire pore-scale three-dimensional optical images of the pore geometry in reservoir sandstones. This technique uses unique properties of coherent light to see through drilling muds and up to a millimeter into the sandstone. This data forms the basis of upscaling experiments to test theories of interfacial area per volume.

2) To construct laboratory micro-models with matched topological properties based on the data from the pore imaging. Interfacial area per volume will be measured directly in controlled imbibition and drainage experiments, together with capillary-pressure-saturation data and relative permeability data. This set of interrelated data will allow rigorous testing of upscaling theories.

3) To perform core-scale experiments of relative permeability and capillary-saturation, and to make metal casts of the pore geometry and interfacial area per volume. This core-scale data (including pore-scale from the metal casts) will be compared with the pore-scale data of the first two objectives, extending the observation scales over four orders of magnitude.

2.0 Experimental

2.1 Optical Coherence Imaging

2.1.1 Experimental Set-up for Imaging on Sandstone Samples

An Optical Coherence Imaging (OCI) system was developed for this project to image into the sandstone. The OCI system (Figure 1) consists of a mode-locked Ti:sapphire laser (120 femtoseconds (fs) pulses with 100 MHz repetition rate), a modified Mach Zehnder interferometer with a sample arm and a reference arm, and a photorefractive multiple quantum well (PRQW) device[Nolte, D.D., 1999] that is the dynamic holographic film. An electric field (DC 10 kV/cm) is applied in the plane of the device. This configuration is called the transverse-field geometry that uses the Franz-Keldysh effect. In the interferometer, a de-magnified telescope (4:1) is used in the detecting arm that decreases the beam diameter to 1.0 mm on the sample. As a result, the intensity increases about 16 times at the sample. Two lenses with the same 150 mm focal length are separated by twice the focal length to form a 4-F system prior to the PRQW device (Figure 2).

In this 4-F system, the sample is placed at the focal plane in front of the first lens and the PRQW device is placed at the focal plane in back of the second lens (Figure 2). The plane that is halfway between the lenses is called the Fourier plane or the transform plane. The 4-F system projects a 1:1 image of the sample onto the holographic film. A spatial filter is located at the Fourier plane of the 4-F system to reject part of the scattered light from the sample, and allow the ballistic components to travel to the device. The signal beam interferes with the reference beam when the optical path lengths between the signal and reference arms are matched to within a coherence length of the laser by adjusting the translation stage in the reference arm. The interference fringes are imprinted onto the holographic film. The holograms are reconstructed using a degenerate four-wave mixing configuration. The first-order diffracted signal from the reference beam is imaged onto the surface of a cooled CCD camera (RTE/CCD 1317, Princeton Instruments) with a 150 mm focal length lens, while an aperture is used to cut off the zero order beam. The efficiency of the four-wave mixing is optimized by adjusting the wavelength and bandwidth of the laser, the size and position of the aperture, and the relative intensities between the signal and reference beams.

To obtain information from deep in the sandstone, the system must be sensitive enough to acquire weak images under highly incoherent background. According to our theoretical

analysis, the intensity of the first-order diffraction used to get a hologram in degeneration four-wave mixing can be increased by increasing the reference intensity. However, two limitations must be considered in the experiments when increasing the reference intensity. The first limitation is related to the Joule heating limit of the PRQW device that limits the total intensity on the device. We measured the Joule heating limit intensity to be about 90 mW/cm^2 for the device used in this project. In the experiments during this work period, a total intensity of 60 mW/cm^2 was used. The second limitation is the saturation of the cooled CCD camera caused by scattered light from the edges of the device and scattering defects in the device itself. To reduce the effect of the second limitation, the signal beam can be positioned on the device in regions with fewer scattering defects and edge effects. The signal beam has a diameter of about 0.5mm on the 1.0 mm device. The location of the signal beam can be selected using the region of interest (ROI) function of the cooled CCD camera. With this arrangement, uniform illumination across the entire device window can be achieved.

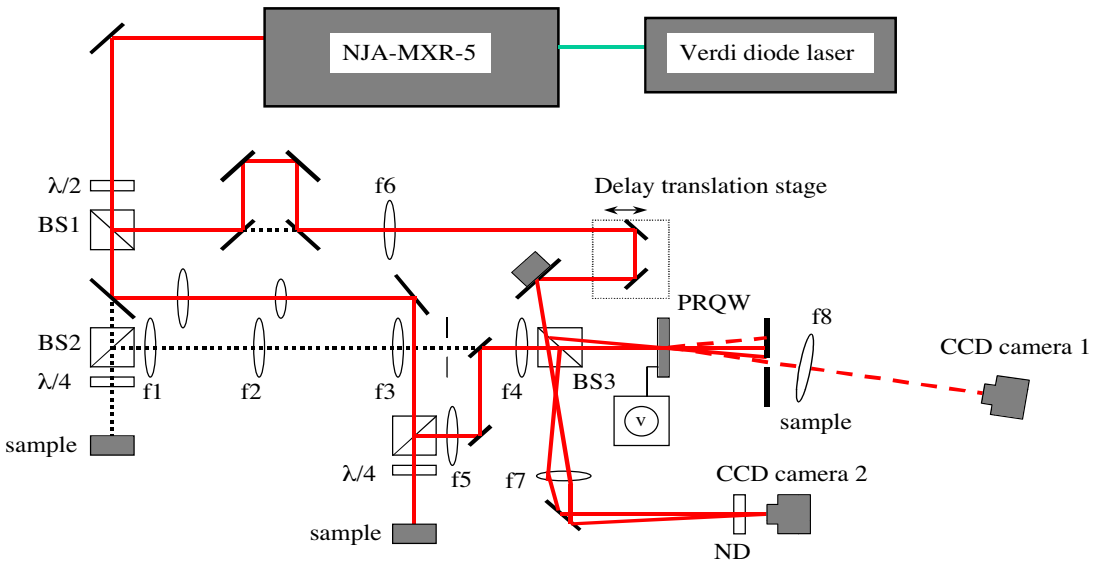

BS1, BS2: polarization beam splitter. BS3: 50/50 beam splitter.
f1=200mm, f2=100mm, f3=150mm, f4=f5=150mm, f6=500mm, f7=50mm, f8=150mm.
ND: Neutral Density Filter

Figure 1. The design and modifications of optical coherence imaging. The solid lines represent the modified setup and the dash lines are from the original setup.

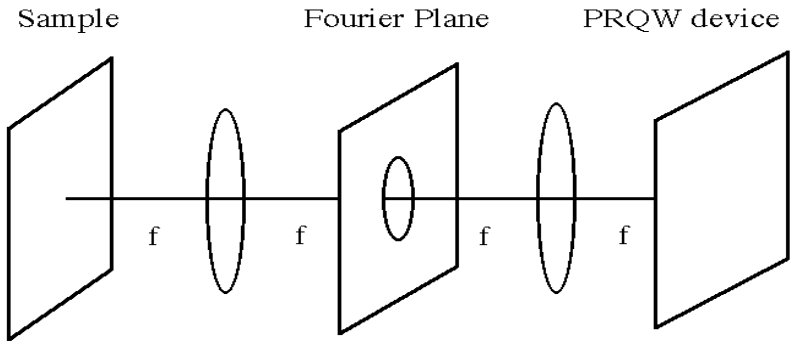

Figure 2. Two lenses form a 4-F configuration to get a 1:1 image between the sample and PRQW device.

2.1.2 Experimental Set-up for Imaging in a Synthetic Borehole

Work during this reporting period included the design and fabrication of an Optical Coherence Imaging device that uses a borescope. A borescope is traditionally used in medicine to examine tissue that is accessible through human orifices (e.g., the lining of the esophagus). One of the objectives of this project is to determine if OCI can be developed to work through a borescope to image sandstone grains in borehole walls in the field (e.g., in oil and gas wells). As the first step toward this objective, we measured the electric field cross correlation by using a borescope in the signal arm of a low coherence interferometer. This measurement is similar to optical coherent tomography (OCT). The electric field cross correlation will give depth information of a translucent sample by the change in optical delay in the interferometer. In the sample, each dielectric discontinuity produces an optical "echo" through coherent backscattering. The results will provide parameters for the OCI.

The borescope setup consists of a low coherence light source, a modified Mach-Zehnder interferometer, and a borescope (Figure 3). A diode laser pumped self-mode-locked Ti:sapphire femtosecond laser is used as the low coherence light source. The main input beam is vertically polarized using a half-wave plate, so that it fits the Brewster window inside the borescope. The intensity in the signal beam after the borescope is 3 times as compared to the one with horizontal input polarization. A 10% beam splitter is used to divide

the main beam into signal and reference. The borescope is placed in one arm of the interferometer and a delay stage controlled by a step motor is in the other arm. The interference from the signal arm and reference arm can be observed only when the path lengths of theinterferometer arms are matched to within the coherence length of the laser. The borescope can guide images from a long working length using a relay lens to reach inside tight working places such as a borehole (figure 4). A 80mm lens is used in front of borescope so that the output beam from the borescope to the sample is almost collimated. Two mirrors in the reference beam are used to overlap the reference beam with the signal

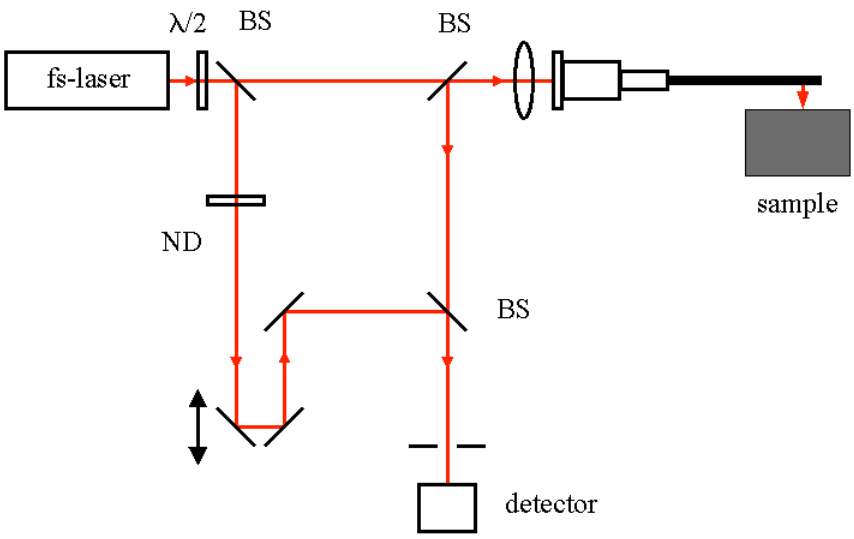

Figure 3. Experimental setup of optical coherent detection using a borescope. BS: beam splitter. ND: neutral density filter.λ/2: half wave plate.

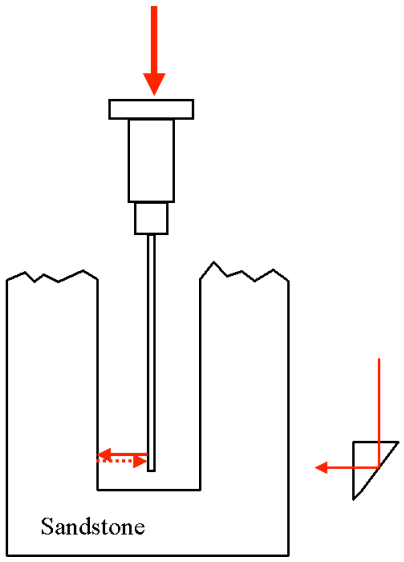

Figure 4. Schematic draw of the borescope

beam. When a mirror is placed at the sample position, ring fringes are formed which are monitored by a CCD camera.

The electric field cross-correlation signals are measured by using a photoreceiver (Newfocus 1801) and a lock-in amplifier. During measurements, a pinhole is placed at center of the ring fringes. Since the signal intensity is very weak for most cases, a chopper is placed in the reference arm for lock-in detection. The time constant of the lock-in is selected to be faster than the time required for the movement of each step in the step motor. Depending on the signal beam intensities, different neutral density filters (NDs) are used in the reference arm in order to get the best modulation depth in the fringes.

The laser profile is monitored using a monochromator. The pulse with a wavelength profile of Gaussian shape is used in the electric field cross-correlation (Figure 5). Since we are doing non-adaptive homodyne detection, we need to consider the problem of laser speckle. The speckles from a filter paper are collected at the detection position with a CCD camera. The size of the pinhole is set to be large enough to cover several speckles of the signal beam figure 6.

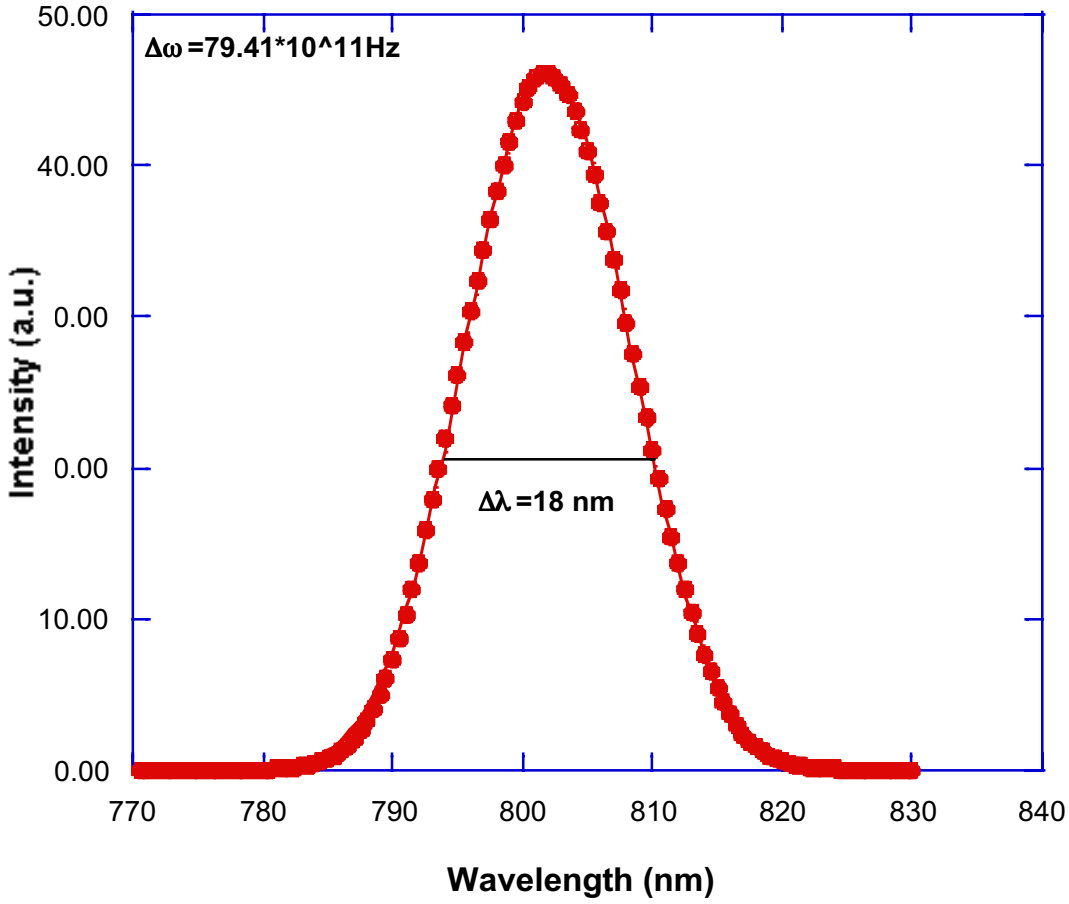

Figure 5. Laser profile measured by a monochromator.

Figure 6. Laser speckles and pin hole.

2.2 MICRO-MODEL

2.2.1 Sample Preparation

This section gives a description of the procedures for performing optical lithography; complete details are given in the manufacturer's manual (Shipley, 1982) and by Thompson, Willson and Bowden (1994).

In optical lithography a pattern is transferred using a visible light image to a photosensitive polymer layer called photoresist. This layer acts essentially as photographic film. When a region of the photoresist is exposed to a sufficiently large integrated intensity of blue light, a photochemical reaction within the photoresist makes the region soluble in a special developer solution (usually just a base). The unexposed photoresist is not soluble, so after development the photoresist layer contains a negative image of the original light pattern. In all of our work we have used Shipley photoresist types 1805 and 1827, and their standard developer (Shipley, 1982). The image has been transferred to the photoresist in two different ways. In one method (Figure 7, left) a photomask is put in direct contact with the photoresist and the exposing light is transmitted through the mask. This mask is typically an opaque metal layer on a glass substrate, or a small portion of an ordinary video transparency sheet onto which the appropriate pattern has been printed. With this contact configuration the mask pattern is transferred in a 1:1 fashion to the photoresist sample; i.e., without

magnification or reduction in size. We use this method for making the coarse (i.e., largest scale) features of the micro-models. The smallest sample features are made by projecting the mask pattern onto the photoresist through a microscope objective. We employ a specially modified optical microscope which enables the image of the mask to be focused onto the sample at the same time as the sample is in focus to the observer. Projecting through a 50x objective yields a 50:1 reduction in the size of the image relative to the scale of the mask. In this way we can routinely achieve sub-micron feature sizes at the sample.

Construction of a complete micro-model involves several steps (Figure 8). The first is to transfer the pattern of the desired flow geometry into a photoresist layer – this is accomplished using optical lithography as just described. The resulting glass substrate/photoresist layer will form the bottom and sidewalls of the final micro-model. The top wall (ceiling) of the micro-model is formed by a second glass coverslip. This "top plate" is bonded to the bottom layer using another layer of photoresist – this bonding is accomplished by bringing the two glass coverslips into contact with gentle pressure (approximately 1 atm, applied in a special holder in which a flexible plastic sheet is pulled against the sample by an applied vacuum) immediately after application of photoresist to the top plate (Figure 8a). The top plate also contains two holes (approximately 1 mm in diameter, drilled ahead of time) that serve as inlet and outlet for the finished micro-model (Figure 8c). The inlet and outlet regions are fairly open spaces (approximately 4 mm on a side) on the micro-model, and contain "pillars" which are approximately 0.5 mm in diameter to prevent collapse of the structure (Figure 8b). The working region of the micro-model is the area labeled as "channel" in Figure 8b. This is where a percolative pattern is created in the bottom photoresist layer.

2.2.2 Flow Measurement Apparatus

A schematic of the flow measurement apparatus for the micro-models is shown in Figure 9. This apparatus is used for simultaneous measurements of flow rate and optical characterization of the geometries of the various phases within the sample. This apparatus contains (1) two pressure sensors to monitor the input and output pressures, and (2) a video camera interfaced to an optical microscope to image the two-phase displacements experiments.

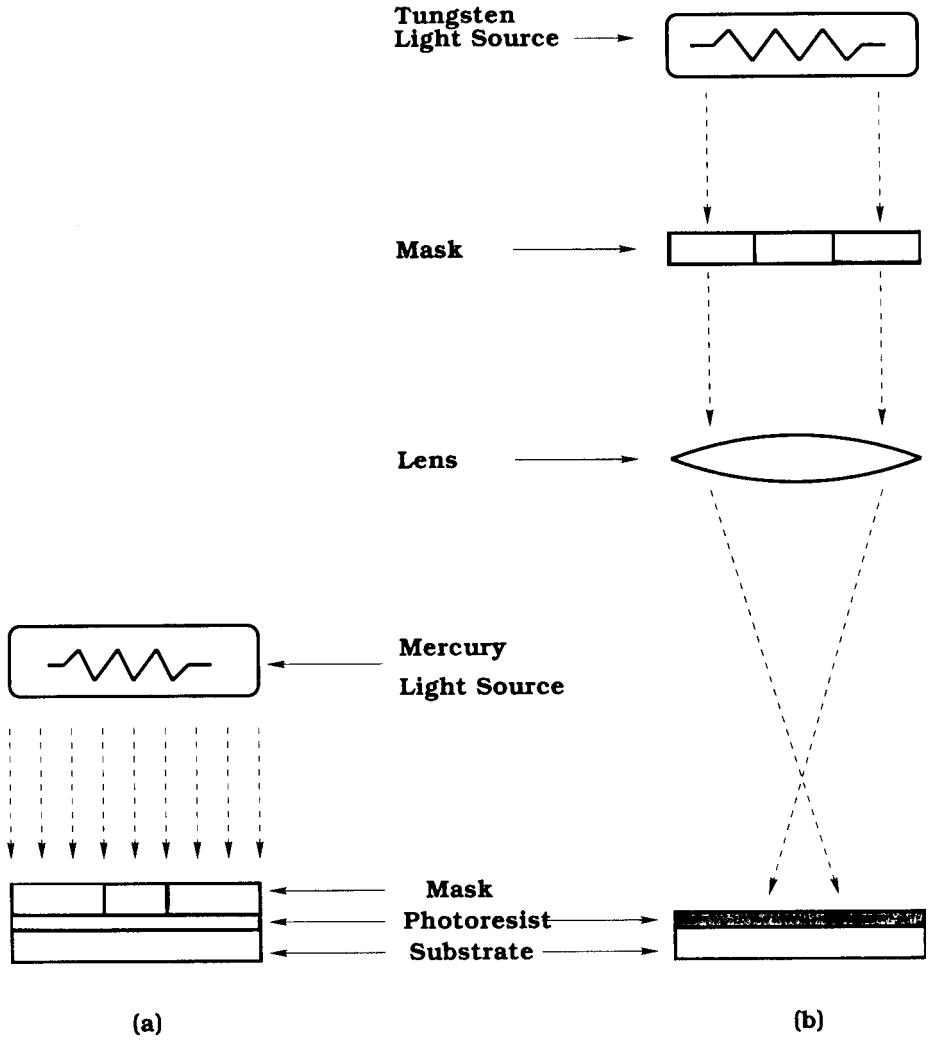

Figure 7. Schematics of the procedures used for optical lithography. Left: contact lithography. Right: projection lithography.

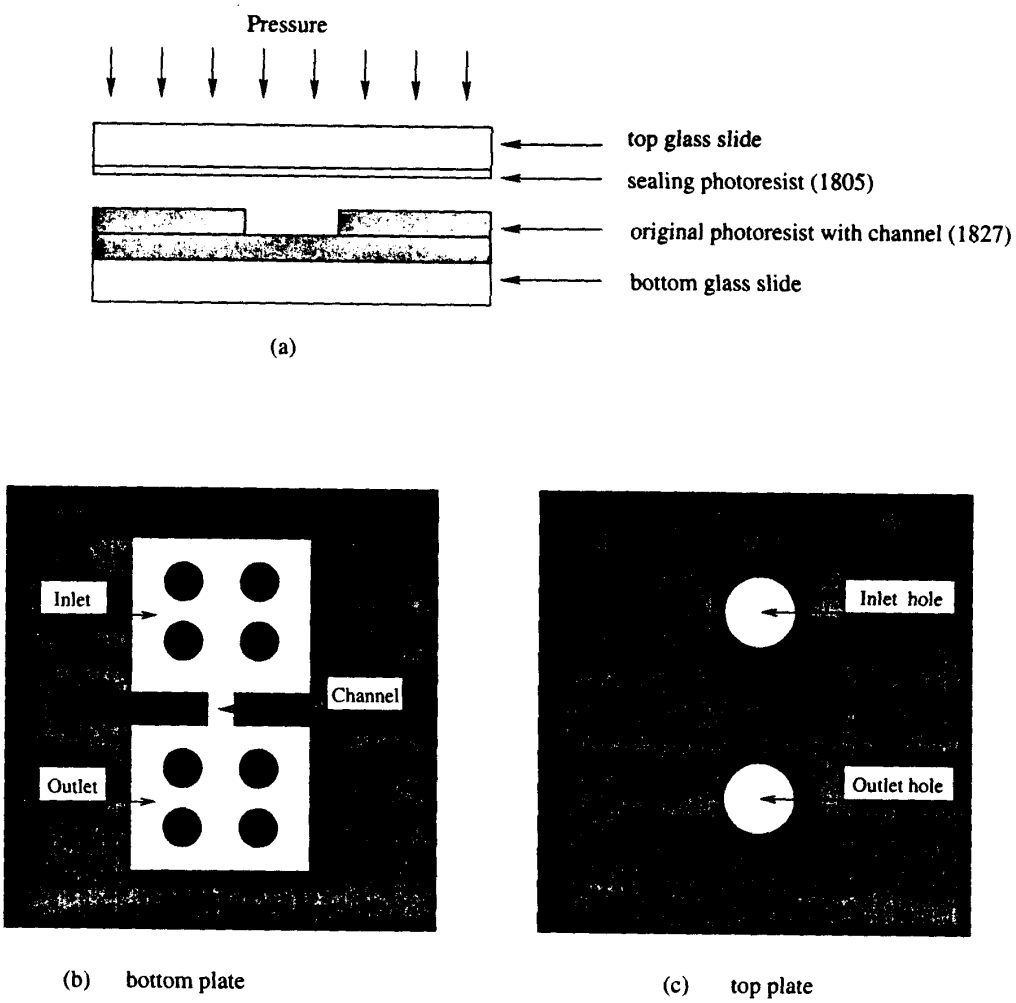

Figure 8. Micro-model layout. (a) Side view showing bottom plate containing micro-model pattern and top plate just prior to bonding. The glass slides are cover glasses 200 microns thick. The photoresist layers are 0.5 micron (type 1805 photoresist) and 2.7 microns (type 1827 photoresist). (b) Arrangement of inlet, outlet, and sample (channel) regions. (c) Inlet and outlet holes are drilled in the top plate.

To perform a flow measurement on a micro-model, the micro-model is initially saturated with a fluid such as silicone oil, which is inserted through the "outlet" region in Figure 9. A second fluid, such as nitrogen gas, is then introduced through the inlet region. The flow rate of this second phase is measured using video microscopy together with an "on-chip" flow capillary. This capillary is a long narrow flow channel that is arranged to be in series with the sample and is located between the sample and the outlet region, as shown in Figure 10. The meniscus of the second fluid is tracked via microscopy as it moves along the measurement capillary, and the flow rate calculated from the known dimensions of the capillary (typically 0.2 mm wide and 2.7 microns deep). This method makes it possible to

measure extremely small flow rates very quickly. All measurements are conducted at room temperature (temperature stability better than 0.5 degree Celsius during a measurement), with the apparatus located within one of the clean bench environments.

The measurement of *IAV* is also accomplished with our video microscopy setup. For this we capture the image of the micro-model and do image processing with the computer interfaced to the camera. The captured image is processed using thresholding techniques to determine the areas occupied by both fluids and the interfacial area, both of which are crucial for our studies.

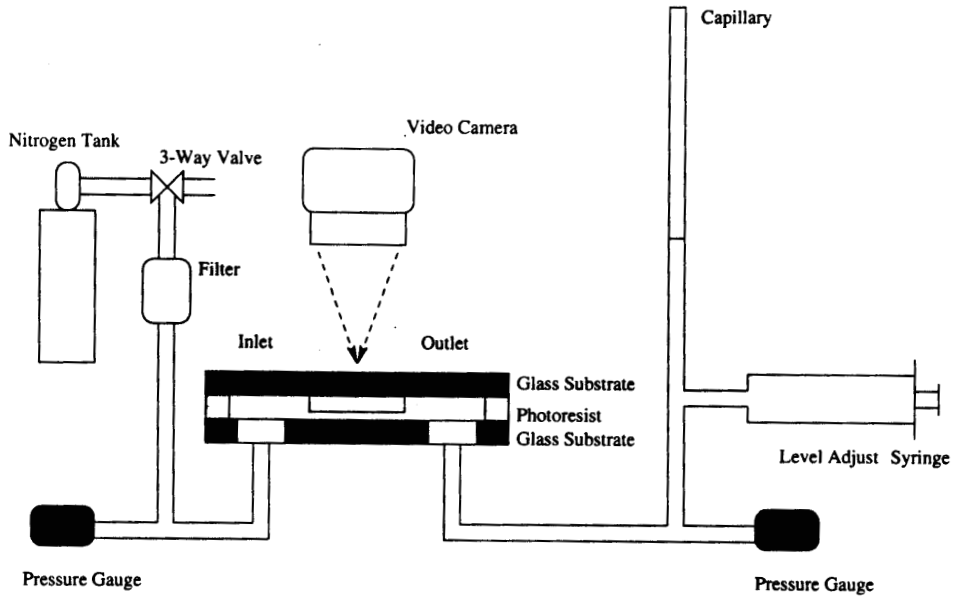

Figure 9. Apparatus used for measurement of flow rates and imaging of fluid geometry within a micro-model. The pressure sensors are piezoelectric sensors (model PX550C1 from Omega Engineering). The video camera system is a SPOT-1 RT color system (Diagnostic Instruments, Inc.) interfaced to a Macintosh G4 computer.

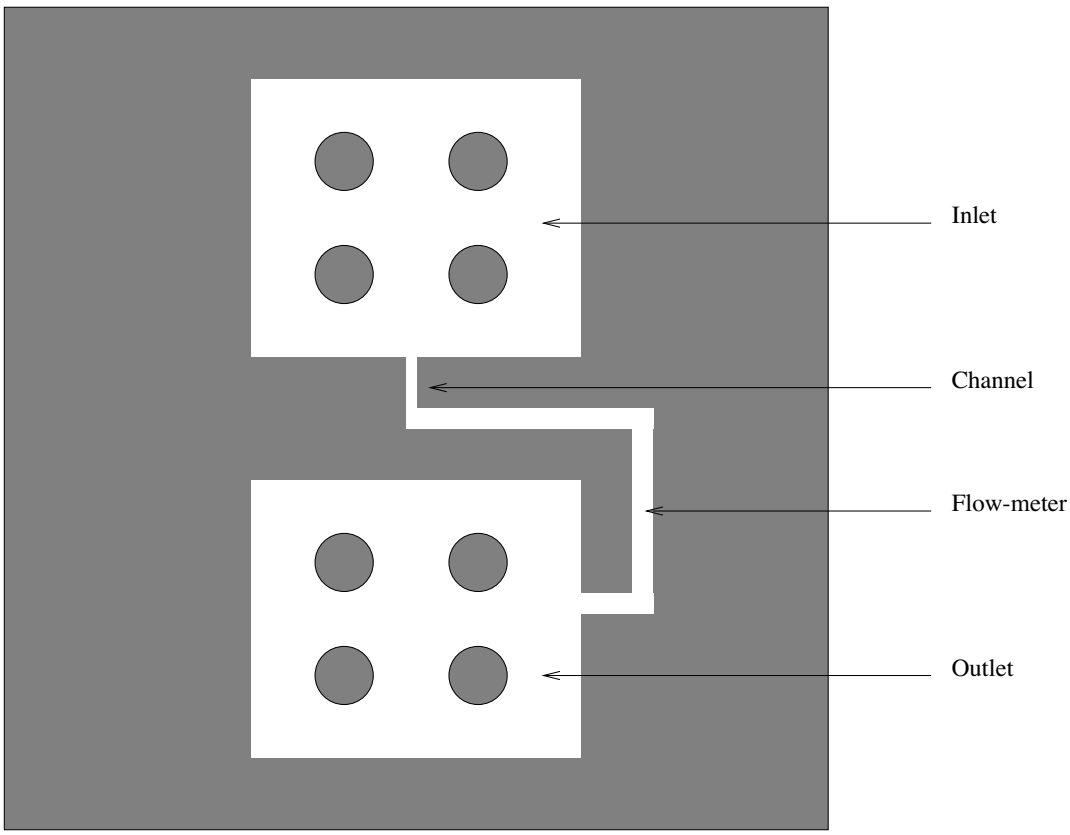

Figure 10. Micro-model with an "on-chip" capillary for the measurement of flow rates. The percolative flow structure is located in the region labeled “channel.”

2.3 WOOD'S METAL INJECTION

2.3.1 Sample Preparation Procedure

2.3.1.1 Sample Preparation for Injection & Flow Measurements

For the measurement of absolute flow rate and for the Wood's metal injection experiments, whole core samples from blocks of sandstone are used. The samples are cored to a diameter of 52 mm and have a length of 94 mm. The samples are coated with epoxy. The purpose of the epoxy is two-fold. First, the epoxy is used to increase the diameter of the sample by 52 mm to provide a competent sealing surface. The second purpose of the epoxy coat is to seal the surface pores of the sample to prevent dominant flow paths forming along the surface of the sample. The procedure for applying the epoxy coats includes: (a) applying a thin layer of epoxy to the surface the sample and letting the thin coat of epoxy harden; (b) placing the thinly coated sample in the center of a tube with a diameter of 104 mm; and (c) filling the remaining space in the tube with more epoxy and letting the epoxy harden. Measurement of the sample porosity is made prior to and after coating with epoxy using a wet/dry method.

2.3.1.2 Sample Preparation for IAV Measurements

After the sample has been injected and post-injection flow measurements have been made, the sample is destructively examined to obtain information on porosity, saturation of the sample with Wood's metal, and interfacial area per volume (IAV). The Wood's metal injected sandstone core is flushed with isopropyl alcohol to remove any remnant ethylene gylcol in the sample. The flushed sample is heated in the oven at a temperature of 54 ^{o}C for several days to evaporate the any remnant isopropyl alcohol. Then, the central portion of the sample is used for the investigation of IAV. The sample is cut to a 25.4 mm by 25.4 mm by 100 mm rectangular prism, and then sectioned into 4 pieces measuring approximately 25.4 mm by 25.4 mm by 25.4 mm. The size of the sample is controlled by the sample holder of the Scanning Electron Microscope (SEM). After cutting of the sample to the required size, the surfaces (perpendicular to the global flow direction during injection) of the four sections are polished on a polishing wheel (15 micron powder size) to create a flat polished surface.

2.3.2 SEM Scanning Procedure for Sandstone Samples

Using a Scanning Electron Microscope enables the collection very high magnification images of the pore space and metal-filled pore space in the sandstone samples. The SEM used for this project is a JEOL 35CF operated with an accelerating voltage 25kv, an objective aperture setting of #2, a working distance of 39 mm and a condesner lens current of 2.00 to 3.00.

To ignore topographic information from the SEM images, the SEM is operated in a point by point scanning mode using the backscattered (Backscatter Electron Image - BEI) and COMP mode settings. A slow scanning speed is used because the signal is weak and noisy. Digital images are collected with IMIX software installed in a computer, which is connected to the SEM.

The contrast in the resulting image is determined by the material type (atomic number) on the sample surface (Wood's metal, sandstone, air). In the initial testing, the sample was injected with epoxy after being injected with Wood's metal. The epoxy-filled portions of the pore space represented the location of the ethylene gylcol. For samples with a high saturation of Wood's metal, it became difficult to inject epoxy into the sample. The epoxy injection step of the procedure has been eliminated. This requires us to assume that any portion of the pore space not filled with Wood's metal would be filled by a wetting phase.

2.3.3 Wood's metal Injection Procedure for High Injection Pressures

Wood's metal injection experiments were performed on several sandstone samples at high injection pressures (i.e., greater than 34.5 kPa). The following procedure was used for Wood's metal injection experiments for injection pressures greater than 34.5 kPa:

1. Place Wood's metal tank (Figure 11). Mount the sample in holder and install sample in the other tank and seal. Fill the holding tank with paraffin oil. Close valves 1, 2, 3, 4, and 5. Place flexible heaters on the outlet tubing leading to sample and the chamber on the tubing. Monitor the temperature and pressure of the whole system.

2. Increase the temperature of the paraffin oil to 90 °C. Once a temperature of 90 °C has been achieved, maintain the temperature four hours before Wood's metal injection.
3. Apply 137.9 kPa gas pressure to Wood's metal tank. Open valves 1 and 4. Open valve 2 to let melted metal flow into sample tank until the sample is completely covered by metal as indicated by the level detector.
4. Close valves 1 and 2. Heat the outlet tubing and chamber to around 90 °C.
5. Apply desired gas pressure to sample tank. Open valves 1 and 4 for metal injection. Use scale to monitor ethylene glycol flow rate. Adjust gas pressure during the injection to maintain a constant pressure. Turn off valve 1 when steady ethylene glycol flow is reached while maintaining the pressure in sample tank. Stop heating the outlet tubing and chamber.
6. Open valve 3. Open valve 2 to let metal flow from sample tank to Wood's metal tank while the pressure in sample tank is maintained at the desired value. Let the metal flow until the sample is not in contact with the metal (based on level detector).
7. Drain paraffin oil from the holding tank and let the system to cool down.
8. Relieve gas pressure when temperature is lower than 50 °C. Open sample tank and remove sample out for further experiments and measurements.

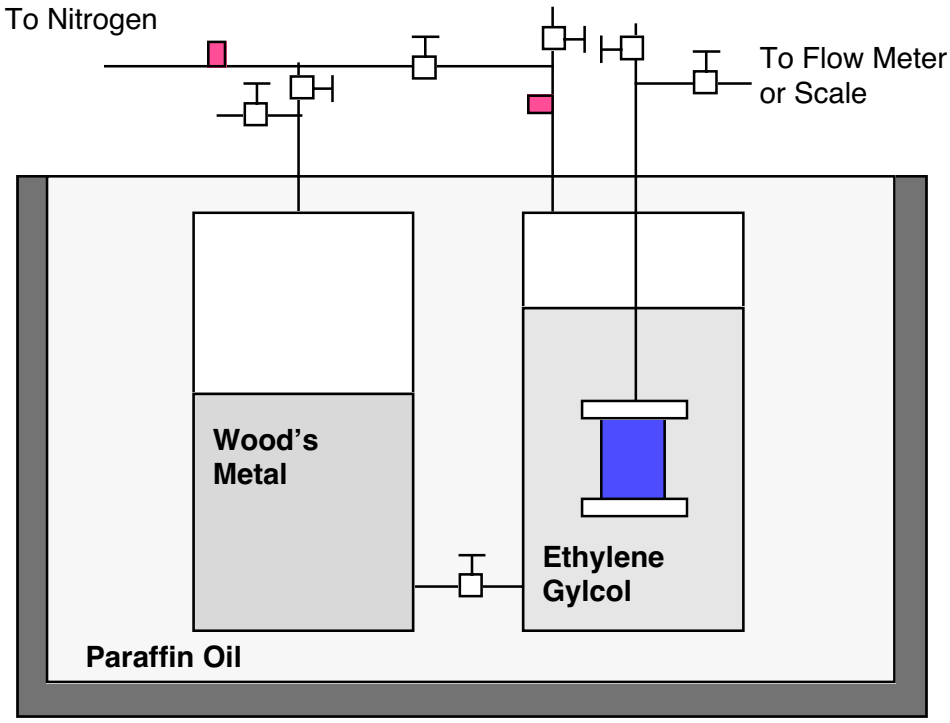

Figure 11. Schematic of Wood's metal injection system.

2.3.4 Wood's metal Injection Procedure for Low Injection Pressures

For low injection pressures (less than 34.5 kPa), the time needed to reach equilibrium would require on the order of several months per sample for samples 100 mm in length. Results from earlier experiments for this contract showed that saturation of Wood's metal with depth in the sample (i.e., parallel to the long axis of the core) did not vary significantly. Thus, we concluded that samples with one-quarter of the length could be used for experiments where low injection pressures are used to reach equilibrium in a reasonable time frame. To achieve low injection pressures, the Wood's metal injection system was re-configured as shown in Figure 12.

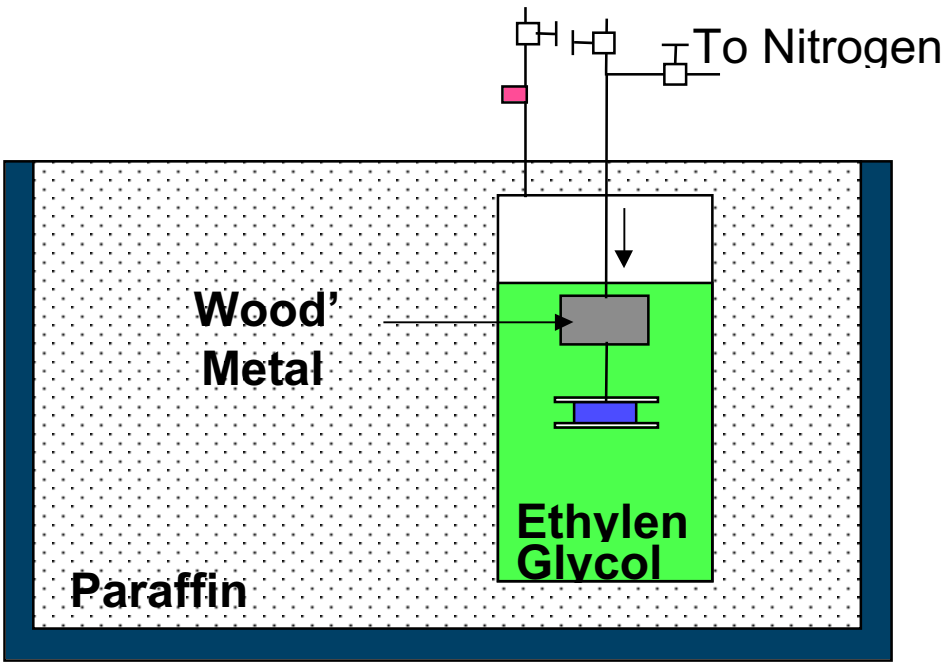

Figure 12. Wood's metal injection system for low injection pressures (i.e., less than 34.5 kPa)

For the low injection pressure experiments, only one confining pressure vessel is used. The confining vessel is filled with ethylene gylcol which is used to vacuum saturated the sample with a wetting phase (ethylene gylcol) and is the medium to transmit heat to the sample. After vacuum saturation, the system is heated to 95 °C. A chamber above the sample (Figure 12), contains Wood's metal. The height of the Wood's metal above the sample is used to create the injection pressure (i.e., the pressure is equal to the density of Wood's metal times the acceleration due to gravity times the height above the inlet) in addition to an applied Nitrogen pressure of a 6.9 kPa. The injection procedure continues until equilibrium is reached. Approximate injection time for low pressure was estimated following post flow data. The flow rates at low pressures are vary low. The height of the remaining Wood's metal in the chamber is checked to determine the pressure.

3.0 Results and Discussion

3.1 Optical Coherence Imaging

For this reporting period, the results presented represent the initial experiments to test the basic optics of the borescope for performing Optical Coherence Imaging (OCI) through a borescope. The next two sections describe the results and give a short discussion on preliminary operation of OCI through a borescope.

3.1.1 Electric Field Cross-Correlation of Mirror.

To align the system and characterize the depth resolution, a mirror is used in the signal beam to record the electric field cross correlation. Normally, there are multiple reflections from lens surfaces, neutral density filters, and beam-splitters, but a major part of those reflections can be separated from the mirror reflection by careful alignment. However, there is a part of incoherent background that still remains, which could be a serious problem in the detection of weak signals. In the case of holographic OCI, although the background is separated from the diffraction signal, the scattering from device edge and scatters inside the device window could reduce the dynamic range of the CCD camera. Therefore, reducing and quantifying the incoherent background is very important.

Figure 13 shows the electric field cross correlation from the mirror. A long distance scan (more than 4mm) shows only one peak at the path matching position. The baseline decline comes from walk-off of the reference beam. The insert curve is a detailed scan around the peak. FWHM of this peak gives depth resolution of the coherent detection.

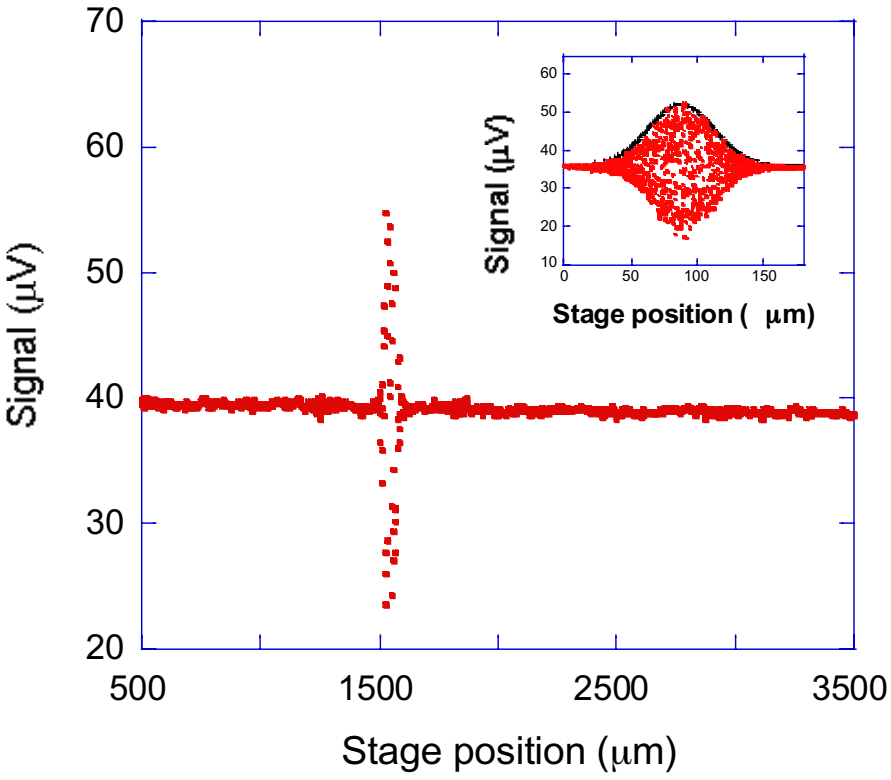

Figure 13. Electric field cross correlation of a mirror. Inset curve is acquired with a small step that shows a Gaussian shape peak.

3.1.2 Electric Field Cross-Correlation of Paper.

To properly simulate the optical coherent detection of highly scattering samples, we measure the electric field cross correlation from different types of paper. There are two kinds of signals we want to detect. One is weak mirror reflection hidden inside strong incoherent background. In this case, the "echo" structure will be quite simple and the results should be similar to mirror reflection except different dynamic range of detection. Another is small angle single scattering. In this case, the collection angle of the borescope will be related to the coherence and incoherence ratio in the signals. In our present setup, the distance between the borescope and the sample is about 30 mm, and the laser beam is almost collimated by using a lens at the input of the borescope. Considering a 2 mm window at the end of the

borescope, the setup has a very small collection angle, which provides further useful information for borescope OCI.

Figure 14 shows the electric field cross correlation of a filter paper. The input power in front of the borescope is about 200 mW. The signal detected from the paper in the lock-in amplifier is about 30 μV. In comparison to the 30 mV of the signal from the mirror, the signal intensity from the filter paper is too weak so for a good contrast we need to decrease the reference intensity to 0.1% using a 3ND. The "echoes" in the figure could be due to the multiple reflections from the top and the bottom surfaces of the paper, or due to scattering from some structures inside the paper such as fibers. On the other hand, the background noise is different for the coherent gates above and below the paper surface. The increase in background noise below the paper surface may be due to scattering from small scatters inside the paper. The electric field cross correlation of a wax paper is shown in figure 6. Unlike the result from the filter paper, the "echo" from the wax paper shows a single peak and is similar to the one from the mirror.

With all the components determined we can calculate a coherence fraction (CF) defined as the ratio of coherent light in the signal beam: $CF=P_{coherent}/P_{signal}$. Coherence fraction for mirror in the signal beam was ~13%. In the case of the filter paper it is 0.01% and 0.6% for the wax paper. Higher CF value in the wax paper is due to mirror reflection from the sample. Using the same technique we measured the coherence fraction for random phase screens with different diffusing angles.

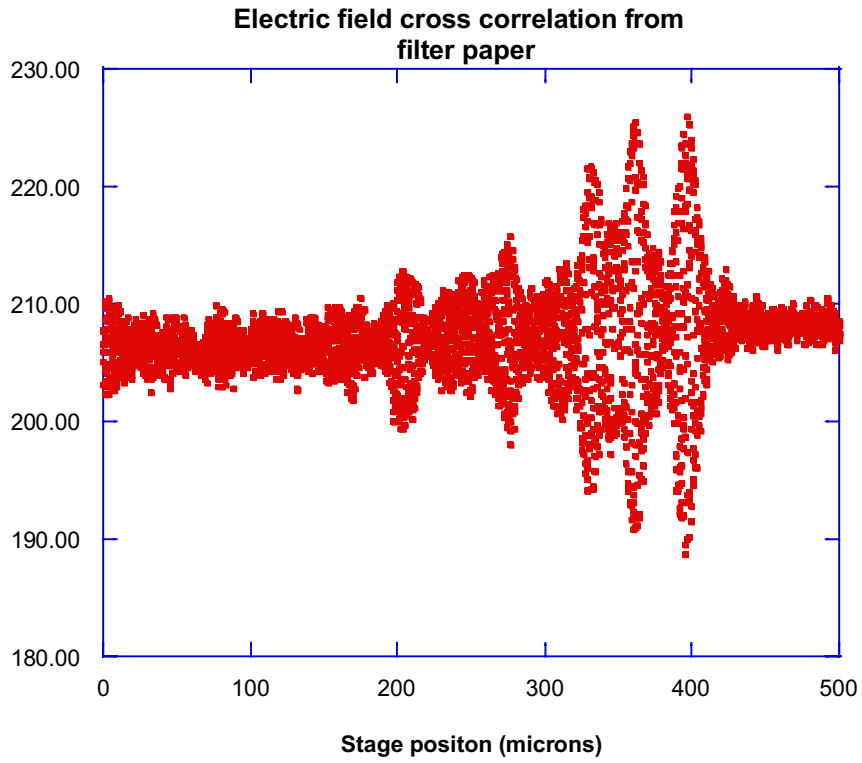

Figure 14. Electric field cross correlation of a filter-paper.

3.2 MICRO-MODELS

A key and unique aspect of our work is the ability to obtain very high resolution optical images (one micron per pixel) of the fluid phases as they invade or are forced from the system. During the period covered by this report we have worked hard to improve the quality of these images, allowing detailed quantitative analyses using powerful image processing software (IDL). This has allowed us to make the first measurements of the area of the interfaces separating the various phase, commonly referred to as the interfacial area per unit volume of sample, *IAV*. In our case, with the flow patterns being really two dimensional, this is really the interfacial area per unit area, but to be consistent with common usage we will still use the term *IAV*. Ours are the first experimental measurements of the *IAV* in any system.

Figure 15 shows some typical images of nitrogen gas displacing the fluid decane. The micro-model geometry was an uncorrelated fractal generated using the algorithm of Nolte and Pyrak-Nolte (1991, this is described in our previous report). This sample was initially saturated with decane. Then nitrogen gas was allowed to invade by the application of pressure. This pressure was increased in stages, with the system allowed to equilibrate for several minutes between each pressure step. Eventually, after on the order of 30 pressure steps (further details of the pressure steps will be given below), the nitrogen gas formed a continuous (geometric) phase across the sample, and flow began. Beyond this point, there was no further change in the geometry of the nitrogen and decane regions. However, there was still decane trapped in the system, in small isolated pockets. Decane was then allowed to re-enter the system, again by the application of pressure. The pressure was increased, in the same manner, and eventually decane could flow through the system.

Such drainage-imbibition cycles were traversed repeatedly for each sample. An example of one such cycle is shown in Figure 15. The upper left photo shows the system just after nitrogen has begun to invade – here nitrogen is the bright phase, while decane and the inaccessible regions of the micro-model are darker in color. Note that even though nitrogen is just beginning to invade, there are isolated pockets of nitrogen which are left behind from previous drainage-imbibition cycles. As we move from the upper left, to upper right, to lower left and finally the lower right photo, the nitrogen is displacing more and more of the decane.

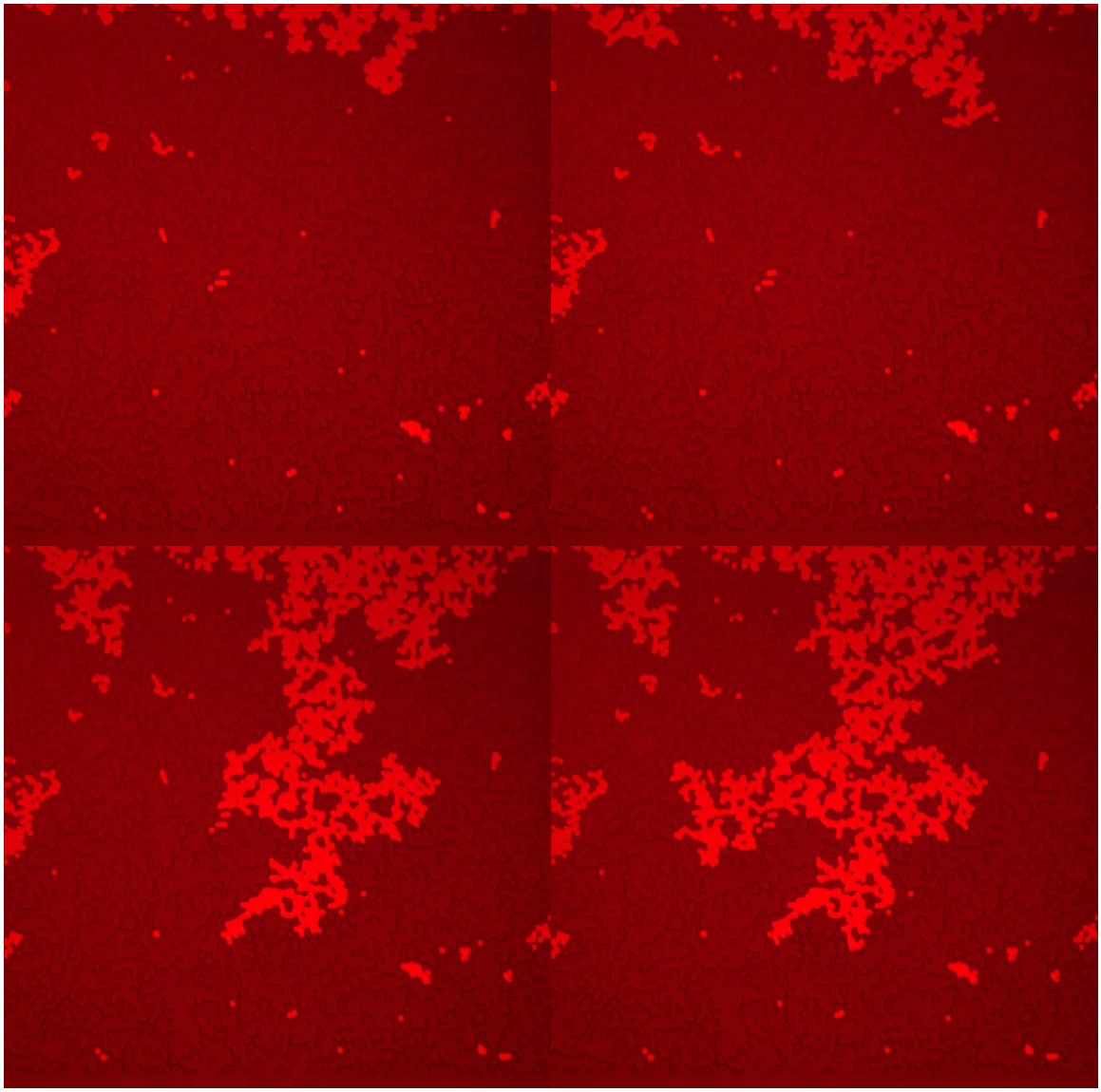

Figure 15. Photomicrographs of nitrogen gas (the brightest phase) as it displaces decane. The darkest regions are inaccessible to decane, while the phase of intermediate optical density is decane.

These drainage-imbibition cycles can be considered more quantitatively using a plot of capillary pressure, P_{cap} , as a function of saturation, S. Here P_{cap} is the nitrogen pressure and S is the fraction of the accessible space which is filled with decane. The different symbols in Figure 16 show successive cycles for the sample considered in Figure 15. Within each cycle the pressure was increased in steps, and then held constant for of order 5 minutes before taking a photograph (as in Figure 15) from which the value of S was obtained. Different cycles could be realized by changing the size of the pressure steps and/or changing the speed

with which the pressure was changed. However, after changing the pressure and then waiting for several minutes, so even though the system was extremely stable, these are not true "equilibrium" curves

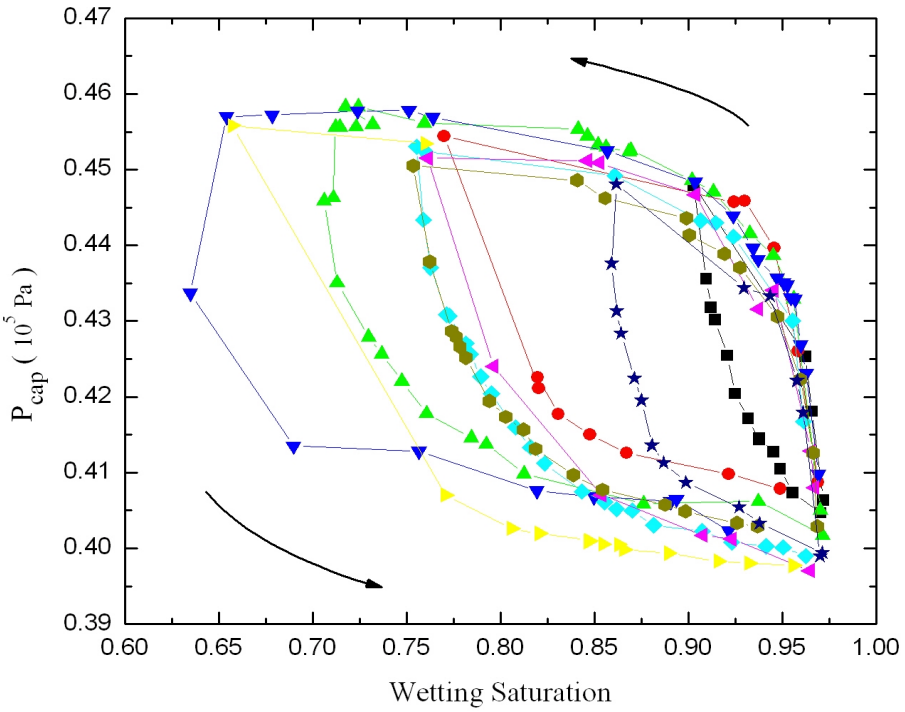

Figure 16. P_{cap} versus S for a series of drainage-imbibition cycles for the sample in Figure 15.

It is clear from Figure 16 that the system exhibits considerable hysteresis when viewed as a function of only P_{cap} and S. However, it would be of great interest if one could construct a "state function" which provided a unique and reversible description of the flow properties. It has been proposed by Gray and coworkers that considering also the *IAV* can yield just such a description. The theoretical arguments of Gray and coworkers provide a general justification for such a description, but they are not rigorous, nor do they actually calculate the *IAV* function. Hence, our studies of *IAV* have two objectives. First, does the *IAV* provide a state-function-like description of the flow properties, and if so, what does this function look like.

To address this question, Figure 17 shows the *IAV*-P_{cap}-*S* surface obtained from the data in Figure 16. This surface was constructed using 3-D plotting, which interpolates to provide a visually connected surface. In order to clarify the nature of this surface, the yellow symbols show the actual data points. We see that the *IAV* surface does indeed appear to be a smooth, single valued surface. Most significantly, there are a number of places where the system had the same, or nearly the same, values of P_{cap} and *S*, but the actual geometrical arrangement of the two phases was quite different, as determined through visual examination of the corresponding photo-micrograph of the system. Even so, the value of the *IAV* in such cases was the same, to within the typical 5% experimental error in analyzing the photo-micrographs. This provides strong support for the predictions of Gray and coworkers.

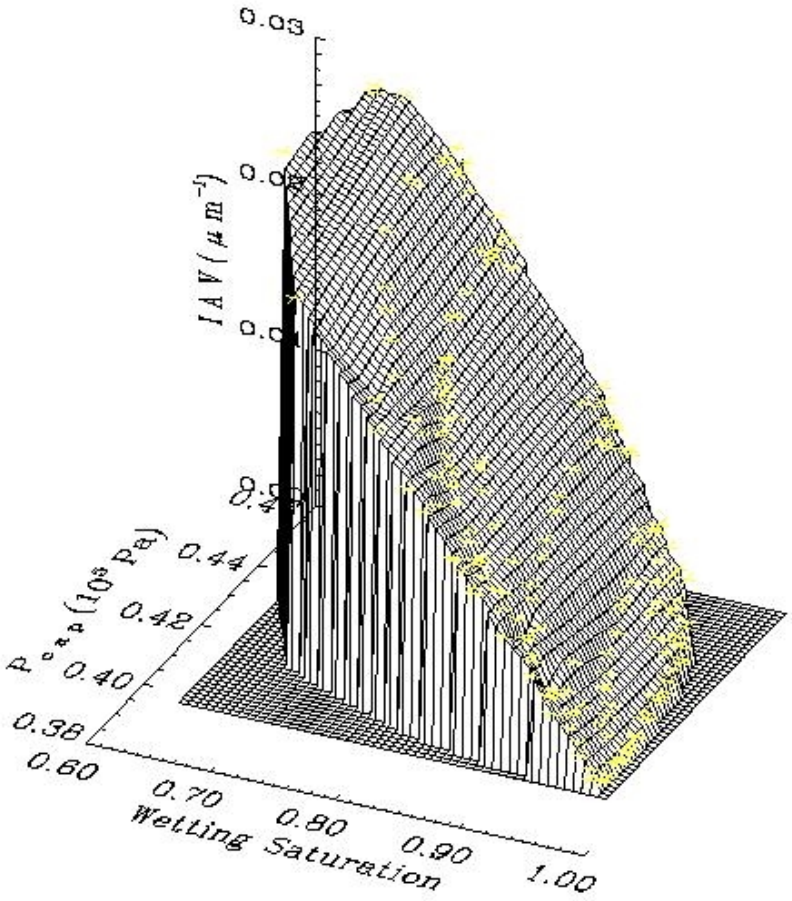

Figure 17: IAV-Pcap-S surface for the uncorrelated micro-model considered in Figure 15.

To investigate the nature of the *IAV* surface, we have measured the surfaces for more than a dozen correlated and uncorrelated micro-models. These are quite laborious measurements, since each data point (e.g., in either Figure 16 or Figure 17) requires the acquisition and analysis of a separate photo-micrograph. Our results indicate that for a given type of micro-model (i.e., either a correlated or uncorrelated fractal pattern) the *IAV* surface is very similar, where by the term "similar" we mean that the magnitude of the IAV is the same at the 10-20% level. However, there does appear to be a significant difference between the two types of models. Figures 18 and 19 show P_{cap}-S cycles and the *IAV* surface for a correlated micro-model. The most notable difference is in the overall magnitude of the *IAV*. For the correlated micro-model it is smaller, by about a factor of 2, than that found for the uncorrelated case.

This can be understood, qualitatively, from the photo-micrograph in Figure 20, which shows an example of the correlated micro-model when the nitrogen has penetrated completely across the sample. Because of the correlated nature of the system, the nitrogen and decane regions are not as finely divided as in the uncorrelated case, and this apparently leads to a smaller *IAV*.

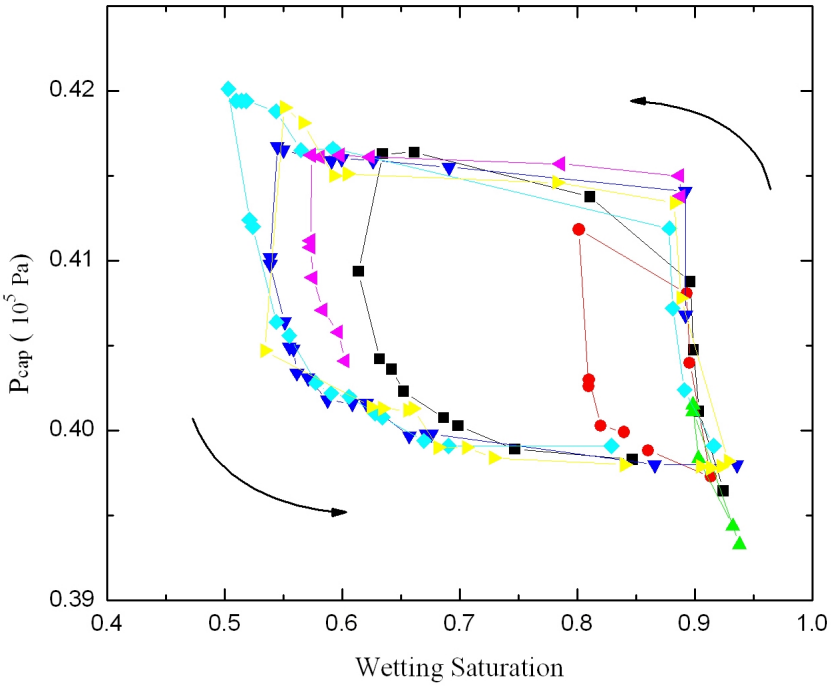

Figure 18. Drainage-imbibition cycles for the correlated micro-model shown in Figure 20.

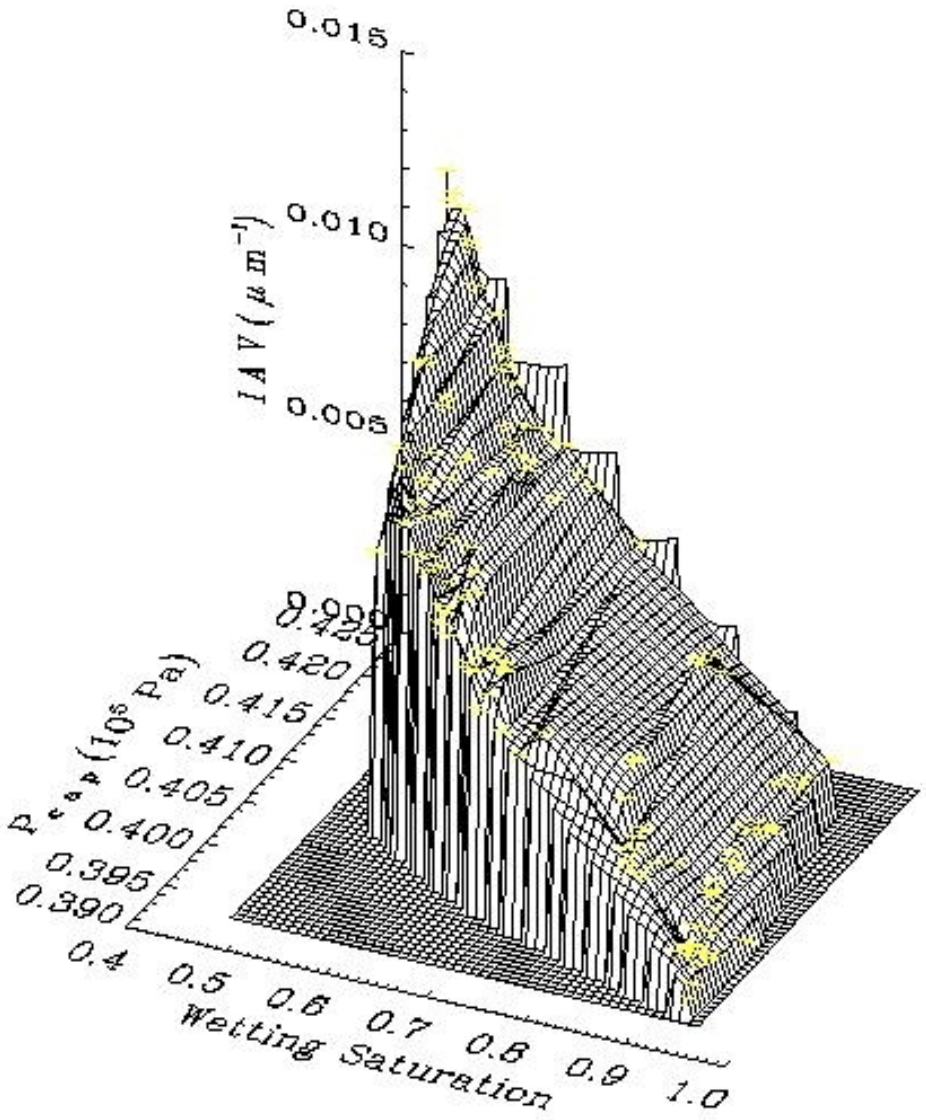

Figure 19. *IAV* surface for the correlated micromodel shown in Figure 20.

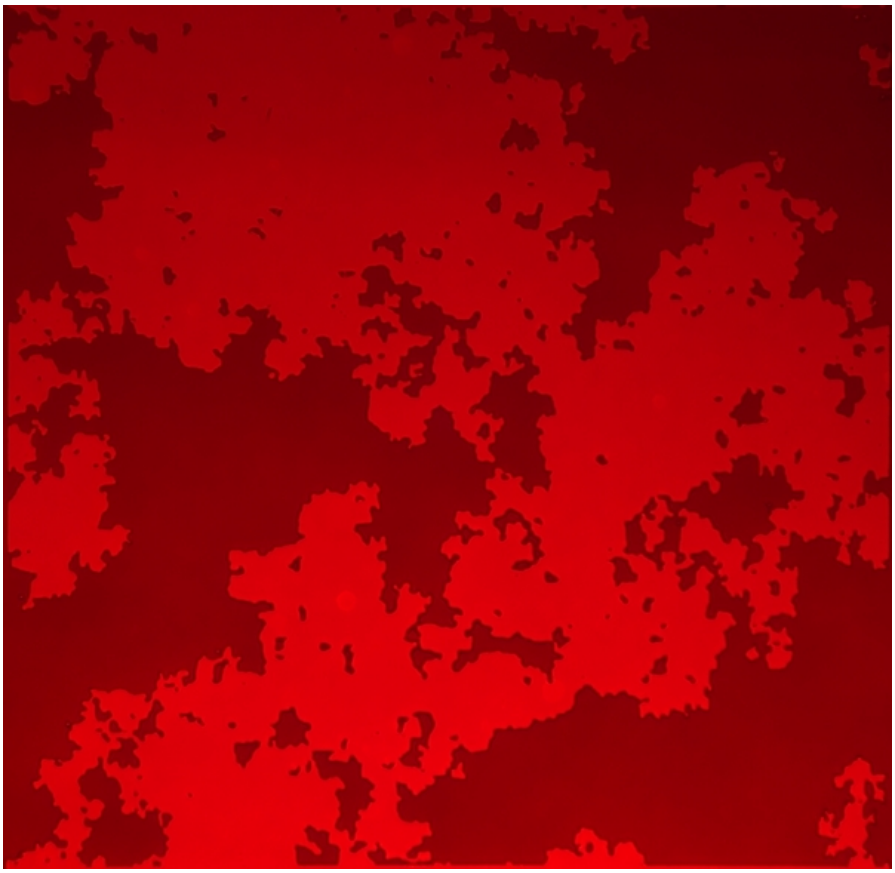

Figure 20. Correlated micro-model. The bright region is nitrogen gas. The dark regions are decane or the inaccessible regions of the system (the contrast makes it difficult to distinguish these two regions).

3.3 Wood's Metal Method

A goal of the Wood's metal injection experiments is to acquire interfacial area per volume (IAV) data for sandstone cores. This requires destructive sectioning (see section 2.3.1.2) of the core after the sample has been injected with Wood's metal. To find reliable IAV values, images of the sample are needed from which the different phases filling the pore space can be discerned.

3.3.1 Image Analysis for IAV

After acquiring SEM images from the Wood's metal injected sandstone samples for several depths and locations, the images are processed to identified the various phases in the sample. A custom code is used to threshold the images for each of the phases. The number

of phases is three (air-Wood's metal – sandstone, or Wood's-metal – epoxy – sandstone). First the saturation and the edge length of each phase, S1, S2, S3, L1, L2, L3 are obtained. Then based on the assumption that each phase contacts with either the second or the third phase, we can calculate L12, L13, L23, the edge length between every two phases following some simple relations:

$$L12=(L1+L2-L3)/2$$
$$L13=(L1+L3-L2)/2$$
$$L23=(L2+L3-L1)/2.$$

From our previous study performed under this contract, the error in the value of edge length from image analysis is 10 percent. In this report, all values of IAV reported for the sandstone samples will be shown with 10 percent error bars. The values of area fractions from image analysis are accurate to within one percent.

3.3.2 IAV Results

Unlike the micro-model experiments (see section 3.2), one Wood's metal experiment and the subsequent image analysis, produces one data point for the interfacial area per volume, saturation and capillary pressure curve. In the micro-model experiments, one experiment can produce a 100 points of data.

We analyzed the images obtained from the samples listed in Table 1. Table 1 lists the sample name, the porosity of the sample, the injection pressure, and the estimated minimum aperture (pore radius) penetrated by the Wood's metal. The estimated minimum aperture is based on the surface tension of Wood's metal (480 dynes/cm) and LaPlace's equation ($Pcap = \sigma \cos \theta / r$, where Pacp is the injection pressure, σ is the surface tension, θ is the contact angle, and r is the radius of the pore).

Figure 21 is a graph of the fraction of pore space saturated with Wood's metal as a function of capillary pressure (i.e., the difference in pressure between the Wood's metal and the ethylene gylcol). Each data point in Figure 21 corresponds to one sample listed in Table 1. There is a sharp transition from the pore space being 10% filled with Wood's metal to being filled with 80% Wood's metal. The difference in pressure between the 10% and 80%

saturations of pore space with Wood's metal is 6.9 x 10^{-3} MPa which corresponds to a 3 micron change in the radius of the pore.

Table 1. Porosity, injection pressure and estimated minimum pore size penetrated for each sample.

Sample number	0	1a	4a	5a	6a	6bs1	6bs3	2bs1	2bs3
Porosity from image analysis (%)	19.4	20.4	20.6	20.4	19.8	18.3	19.6	18.9	18.9
Injection pressure (MPa)	Zero	0.10	0.17	0.34	0.034	0.016	0.021	0.028	0.69
Estimated minimum pore size penetrated (micron)	Not Appl-icable	4.8	2.8	1.4	14	30	23	17	0.7

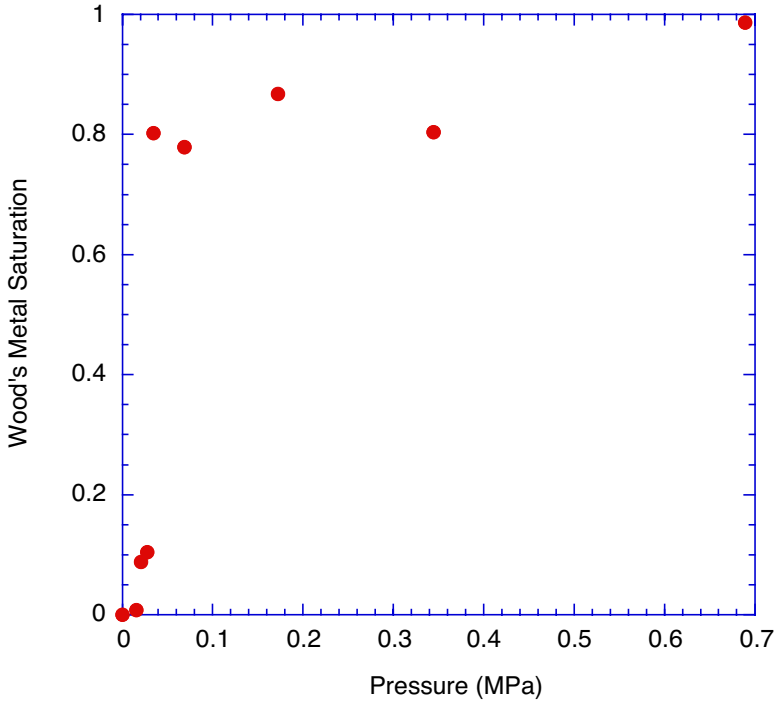

Figure 21. Fraction of pore space saturated with Wood's metal as a function capillary pressure (i.e., the difference in pressure between the Wood's metal and the ethylene gylcol).

Figure 22 is a graph of the interfacial length per area (ILA) as a function of capillary pressure for the samples listed in Table 1. ILA is shown between the solid and non-wetting phase (ILA_{s_nw}, Rock - Metal represented by filled circles), between the solid and wetting phase (ILA_{s_w}, Rock - Ethylene Gylcol represented by the filled squares) and between non-wetting phase and wetting phase (ILA_{nw_w}, Metal - Ethylene Gylcol represented by the half-filled squares). At low metal injection pressures, ILA_{s_w} between the rock and the ethylene gylcol is larger in value than the ILA_{s_nw} and ILA_{nw_w}. From SEM images, it is observed that the surfaces of the sandstone grains are pitted leading to micro-porosity. This micro-porosity appears to be unconnected and is rarely observed to be filled with Wood's metal. By assuming that the micro-porosity is filled with ethylene gylcol, this increases the values of ILA_{s_w} at low injection pressures.

As the injection pressure increases, ILA_{s_w} decreases while ILA_{s_nw} increases as more pores are occuppied by Wood's metal. Figure 21 indicates that the pores are almost completely filled with Wood's metal for a pressure of 0.7 MPa. Because Wood's metal is

never observed in the micro-porosity in the SEM images, ILA_{s_nw} never obtains values as high as ILA_{s_w} at low pressures.

From Figure 22, it can be seen that ILA_{nw_w} (between the metal and ethylene gylcol) is much smaller in value than ILA_{s_w} and ILA_{s_nw}. Figure 23 shows ILA_{nw_w} as a function of pressure. The value of ILAnw_w is close to two orders of magnitude smaller than ILA_{s_w} and ILA_{s_nw}. ILA_{nw_w} never obtains high values because of the sharp transition in Wood's metal saturation as a function of pressure (Figure 21). Conceptaully, ILA_{nw_w} should start out at a low value when the pores are mainly filled with ethylene gylcol (wetting phase) and increase to a maximum value with increasing pressure. After a maximum is reached, ILA_{nw_w} should begin to decrease as the ethlyene gylcol is displaced from the pore space by the Wood's metal (non-wetting phase) under high pressure. In Figure 23, it is not clear if the maximum value of ILA_{nw_w} occurs at 0.034 MPa or at a higher pressure. The data point at 0.17 MPa needs to be repeated to determine if it is correct or is the data point at 0.34 MPa correct. The repeated measurements will determine where the maximum in ILA_{nw_w} will occur for this sandstone sample.

ILA has been hypothesized to be related to both capillary pressure and saturation. For completeness, Figures 24 and 25 show ILA as a function of fraction of pore space filled with Wood's metal. The data in Table 1 represent the results for imbibition experiments. To determine if ILA is uniquely related to capillary pressure and saturation, additional experiments will be performed for drainage conditions.

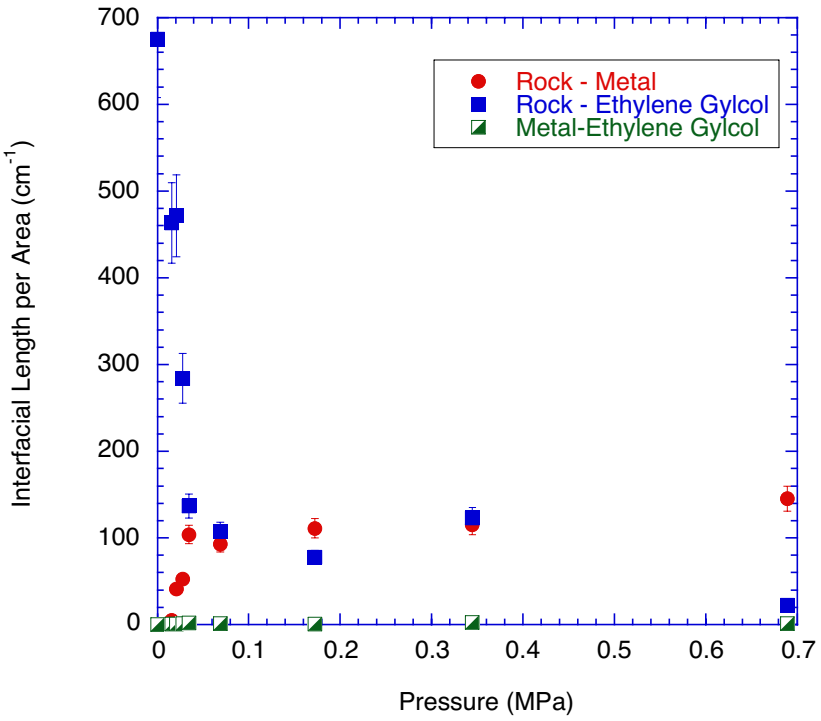

Figure 22. Interfacial length per area as a function of capillary pressure for the samples listed in the Table 1.

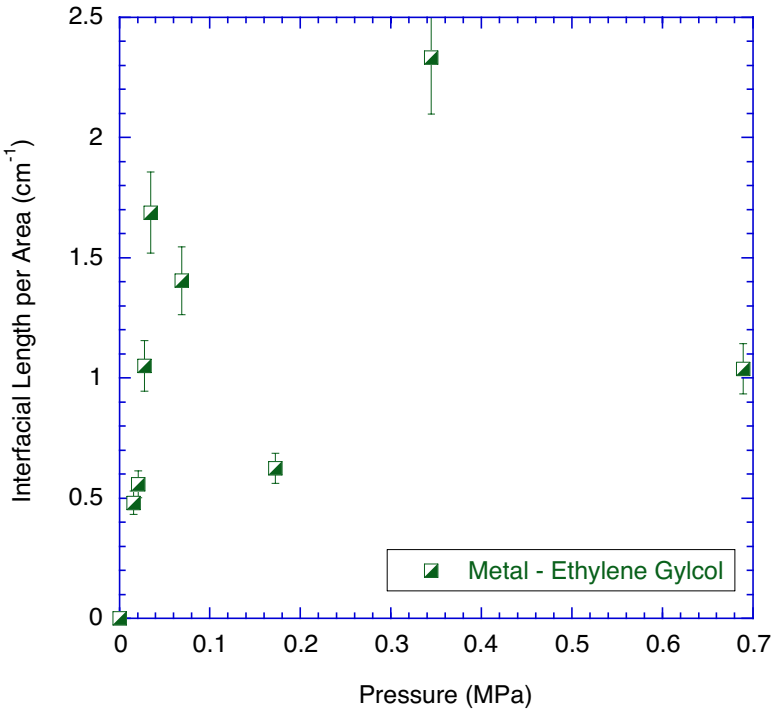

Figure 23. Interfacial length per area between Wood's Metal and Ethylene Gylcol as a function of capillary pressure. This is the same data as in Figure 22 but has been replotted on a more appropriate scale.

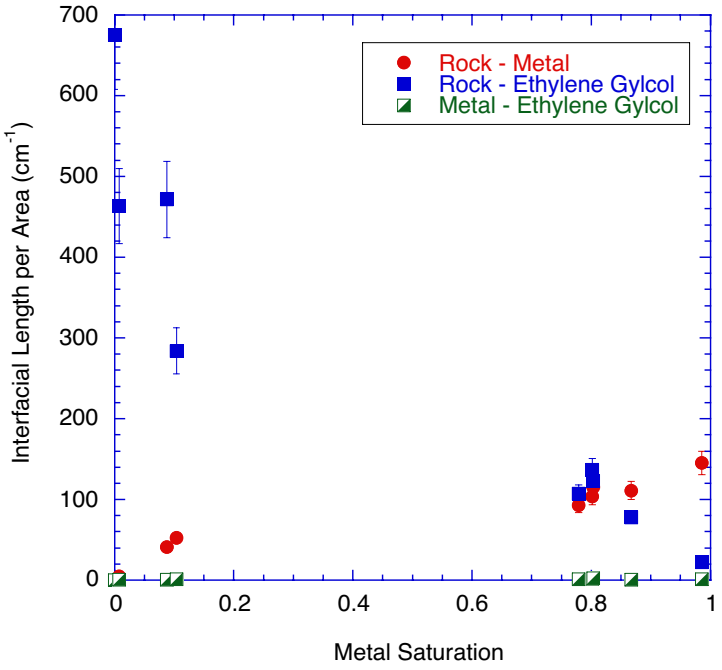

Figure 24. Interfacial length per are a function of fraction of pore space filled with Wood's metal.

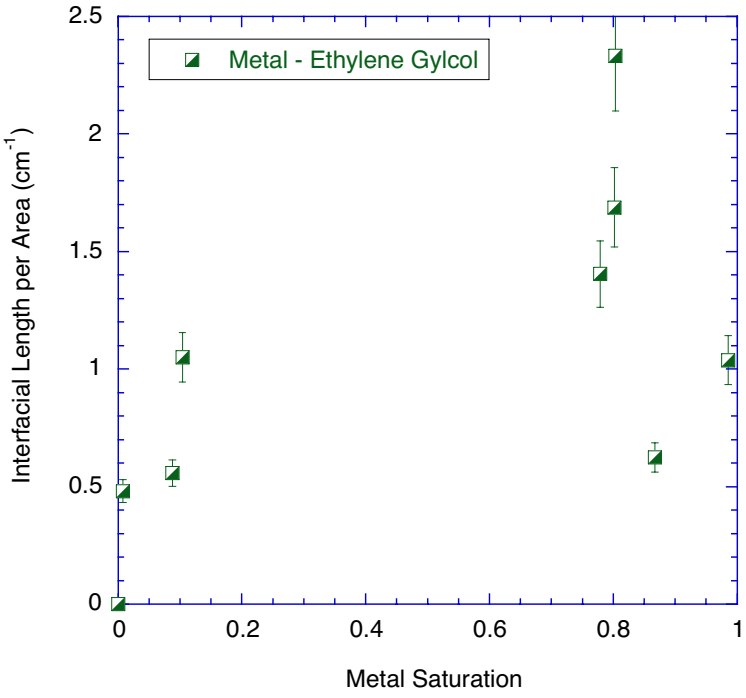

Figure 25. Interfacial length per area as a function of pore space filled with Wood's metal. Same data as shown in Figure 24 but on a more appropriate scale.

4.0 Conclusions and Future Work

4.1 Optical Coherence Imaging

The work with the borescope represents the first demonstration of Coherence detection for potential use in a borehole. The acquired electric field cross-correlation provides information on interfaces in mirror, papers, and diffusers. Future work will determine the ease of using coherence detection through the borescope on sandstone and the difficulty in data interpretation on a natural system.

4.2 Micro-Models

In conclusion, we have obtained the first experimental results for the interfacial length per area, IAL, surface in any system. The results show that, to within our experimental resolution and uncertainties of approximately 5%, this surface is single valued reversible. A better understanding of this surface, especially how it scales with system size and geometry, should lead to more accurate predictions for multiphase flow in porous media.

Future work includes re-analysis of the micro-model data sets. Currently, the analysis of ILA for the micro-models assumes that a film of wetting phase fluid always exist. Thus, ILA_{s_w} is a constant but ILA_{s_nw} is equal to zero. Only ILA_{nw_w} varies with pressure and saturation. A second method of analysis will be developed to determine ILA without the thin film assumption for the micro-models. Under the current system, the length scales for the interface between the solid and wetting phase for the micro-model and the sandstone are comparable (roughly tens of microns). However, the length scales for the interface between the non-wetting phase and wetting phase differ by two orders of magnitude. Additional work will be performed on comparing the ILA-capillary pressure-saturation relationship between two- and three-dimensional systems.

4.3 Wood's Metal Method

The relationship between interfacial area per length (ILA), capillary pressure and saturation for a non-wetting phase and wetting phase in sandstone is essentially completed for imbibition experiments performed on sandstone. Results for two different pressures need to be repeated to determine if the ILA matches conceptual models of the behavior as a function of pressure. The completion of the imbibition measurements were enabled by the reconfiguration of the Wood's metal injection system for low pressures. The data contained in this report represent the first measurements of interfacial length per area on a natural three-dimensional system (i.e., sandstone) under imbibition conditions.

Our future work will be the measurement of IAV on sandstone for drainage conditions. The Wood's metal injection system will not have to be re-configured for the drainage experiments, only the protocol for injection will be altered. The uniqueness of the ILA, capillary pressure and saturation relationship for sandstone cannot be determined until drainage data is obtained. Additional work will be performed on comparing the ILA-capillary pressure-saturation relationship between two- and three-dimensional systems (i.e., the micro-models and the sandstone).

5.0 References

Darcy, H., Determination of the laws of flow through sane, Les fontaines publiques de la ville de Dijon, Victor Dalmont, Paris, 1856, 590-594, (translated and reprinted in Physical Hydrology, edited by R. A. Freeze and W. Back, Hutchinson Ross Publishing Company, Stroudsburg, PA, 1983).

Giordano, N., and J. T. Cheng, Microfluid mechanics: Progress and opportunities, J. Phys. Condensed Matter, **13**, R271 (2001).

Giordano, N., and J. T. Cheng, Interfacial Area, Pore Geometry and Hydraulic Properties from Micro-Models, Milestone Report (DOE Award De-AC26-99BC15207), Purdue University, March 2001.

Gray, W. G., General conservation equations for multi-phase systems: 4. Constituitive theory including phase change, Adv. Water Resources **6**, 130-140 (1983).

Gray, W. G. (private communication, 1998).

Hassanizadeh, S. M. and W. G. Gray, General conservation equations for multi-phase systems: 1. Averaging procedure, Adv. Water Resources **2**, 131-144 (1979).

Hassanizadeh, S. M. and W. G. Gray, Mechanics and thermodynamics of multiphase flow in porous media including interphase boundaries, Water Resource Research **13**, 169-186 (1990).

Muccino, J. C., Gray, W. G. and L. A. Ferrand, Toward and improved understanding of multiphase flow in porous media, Rev. Geophys. **36**, 401 (1998).

Nolte, D.D, and L. J. Pyrak-Nolte, Stratified continuum percolation: Scaling geometry of hierarchical cascades, Phys. Rev. A **44**, 6320 (1991).

Nolte, D. D. ,"Photorefractive Effects and Materials,", (Kluwer Academic Publishers, Dordrecht, 1995).

Reeves, P. C. and M. A. Celia, A functional relationship between capillary pressure, saturation, and interfacial area as revealed by a pore-scale network model, Water Resource Research **32**, 2345 (1996).

Shipley Microelectronic Product Guide, Shipley Co., Newton, MA, 1982

Thompson, L.F., C.G. Willson, and M.J. Bowden, Introduction to Microlithography, 2nd edition, American Chemical Society, Washington, DC, 1994